

# Free Surface Domain Nucleation in a Ferroelectric under an Electrically Charged Tip

Lun Yang\* and Kaushik Dayal†

Carnegie Mellon University

January 12, 2012

## Abstract

This paper examines the process of domain nucleation in ferroelectric perovskites at a free surface due to electrical fields applied through a charged tip above the surface. We use a real-space phase-field model to model the ferroelectric, and apply a boundary element-based numerical method that enables us to accurately account for the stray electric fields outside the ferroelectric and the interactions through electric fields between the external tip and ferroelectric. We calculate the induced domain patterns, the stress and internal electric fields, and the induced surface displacement for various relative orientations of the crystal lattice with respect to the free surface. The effect of the external spatially-inhomogeneous electric field leads to the formation of complex domain patterns and nominally incompatible microstructures. Two key findings are: first, in *c*-axis films, a new domain forms beneath the tip through 180-degree switching and this new domain has the opposite piezo-response as the original domain, leading to a distinct displacement signature on the surface ; and second, in *a*-axis films, domain nucleation occurs at lower applied field because polarization rotates to align with the applied field, whereas in *c*-axis films, the polarization magnitude reduces until 180-degree switching occurs at a higher applied field. We also see that the calculated domain patterns differ significantly from analytical approximations that are often used.

**Keywords:** ferroelectrics; nucleation; microstructure; phase-field

## 1 Introduction

Ferroelectric materials are widely used in sensors and actuators [1, 2]. More recently, they have found applications in high-speed memories [3], and have been proposed as elements of microwave circuits [4, 5] and as photonic switches at small length scales [6]. Many of these modern applications use thin-film geometries with surface electrodes [7]. The edges of the electrodes provide field concentrations that can lead to domain switching. In the context of materials characterization, a charged tip that both induces domain switching and measures the consequent surface distortion is an important and widely-used tool [8], analogous to indentation for mechanical properties. While the applied field and induced distortion

---

\*lunyang@cmu.edu

†kaushik@cmu.edu

are measured/controlled, the detailed process of domain nucleation in the interior cannot be observed. Hence, for all of these applications, modeling and simulation can provide insight into the sub-surface processes of domain nucleation under a concentrated surface field.

In this work, we apply a phase-field model to understand the question of domain nucleation due to a concentrated electric field at the surface. This has been the focus of many experimental efforts, e.g. switching spectroscopy piezoresponse force microscopy (SS-PFM) to detect quantitatively the local switching characteristics [9]. There are also related experiments using light rather than concentrated electric fields [10, 11]. Theoretical analyses to complement these experiments include [12, 13, 14, 15]. However, due to the complexity of the physical situation, analytical approaches necessarily require severe approximations, e.g. linear piezoelectric, and hence computational approaches are an attractive alternative. For example, [16] applied a real-space approach to study the nucleation of domains under a surface electrode. This provided valuable insight into the nucleation process at a surface. However, they make important simplifying approximations on the polarization and electrical field at the free surface. These approximations assume in effect that there are no stray fields outside the ferroelectric. The key point of departure of our work is in the use of a boundary element method for electric field calculations in combination with a real-space phase-field formulation [17, 18]. Our numerical approach enables us to account for the stray electric fields in all of space without making any approximations on their existence or spatial decay. In addition, it enables us to account for the fact that the tip is *outside* the specimen and not in contact with it. We are able to accurately model the tip and specimen together. In addition, in contrast to some of the analytical approaches, the phase-field approach consistently and simultaneously calculates electric field and microstructure in a coupled manner; thus domain nucleation and other events that change the material dielectric response are automatically accounted for.

The paper is organized as follows. We present the phase-field model and the computational method in Section 2. In Section 3, we present calculations of local polarization switching, tip-induced displacement, and induced stress and electric field for different tip strengths in a  $c$  axis film, i.e., with polarization oriented vertically. In Section 4, we examine the effect of free-surface orientation with respect to the crystal lattice. We conclude in Section 5.

## 2 Phase-Field Model and Solution Method

The potential energy  $E$  of a ferroelectric  $\Omega$  with strain field  $\epsilon$  and polarization field  $\mathbf{p}$  is written, following [19, 20, 21]:

$$E[\epsilon, \mathbf{p}] = \int_{\Omega} [U(\nabla \mathbf{p}) + W(\epsilon, \mathbf{p})] d\Omega + \frac{\epsilon_0}{2} \int_{\mathbb{R}^3} |\nabla \phi|^2 dV \quad (2.1)$$

Additional terms from applied electric fields and mechanical loads are present when these are applied, but we do not consider these in this paper. Here,  $U$  penalizes gradients in  $\mathbf{p}$  and models the energy contributions from domain walls, and the stored (Devonshire/anisotropy) energy density  $W$  penalizes  $\mathbf{p}$  and  $\epsilon$  deviating from the spontaneous polarization and strain. The last term is the energy contained in the electric field  $\mathbf{E} = -\nabla \phi$ , where  $\phi$  is the electric potential obtained from Maxwell's equation:

$$\nabla \cdot (\mathbf{p} - \epsilon_0 \nabla \phi) = 0 \text{ over } \mathbb{R}^3, \text{ with given electrode boundary conditions.} \quad (2.2)$$

The first two terms in  $E$  from (2.1) are local to the body being considered, while the electrostatic contribution is over all space. Domain patterns are obtained as local minimizers of  $E$ .

We use tetragonal barium titanate in two-dimensions as our model material. Following [22, 23, 24, 25], we use for the energy:

$$\begin{aligned} U(\nabla \mathbf{p}) &= \frac{a_0}{2} (p_{1,1}^2 + p_{1,2}^2 + p_{2,1}^2 + p_{2,2}^2) \\ W(\boldsymbol{\epsilon}, \mathbf{p}) &= \text{polynomial in } \mathbf{p} + \frac{1}{2} (\boldsymbol{\epsilon} - \boldsymbol{\epsilon}_T(\mathbf{p})) \cdot \mathbb{C} \cdot (\boldsymbol{\epsilon} - \boldsymbol{\epsilon}_T(\mathbf{p})) \end{aligned} \quad (2.3)$$

The details of the polynomial and other constants can be obtained from the references cited above.

These minimizers are numerically calculated by starting with assumed fields  $\boldsymbol{\epsilon}, \mathbf{p}$  and evolving towards a minimum using a gradient descent. The gradient flow of  $E$  in the  $H_1$  norm is [26]:

$$\begin{aligned} \mu_1 \frac{dp_i}{dt} - \mu_2 \frac{d(p_{i,j})_{,j}}{dt} &= \left( \frac{\partial U}{\partial p_{i,j}} \right)_{,j} - \frac{\partial W}{\partial p_i} - \phi_{,i} \quad \text{over } \Omega \\ \left( \frac{\partial W}{\partial \varepsilon_{ij}} \right)_{,j} &= 0 \quad \text{over } \Omega \\ p_{i,i} - \epsilon_0 \phi_{,ii} &= 0 \quad \text{over } \mathbb{R}^3 \end{aligned} \quad (2.4)$$

with  $\mu_1, \mu_2$  both non-negative. Fig. 1 shows the mesh and the computational domain  $\Omega$ . The boundary conditions for the polarization evolution (2.4)<sub>1</sub> are  $\nabla \mathbf{p} \cdot \mathbf{n} = 0$  on all boundaries of the specimen, where  $\mathbf{n}$  is the outward normal to the boundary. The boundary conditions for mechanical equilibrium (2.4)<sub>2</sub> are traction-free on the top surface, and clamped on the other 3 faces. The clamping displacement is set to the value of the stress-free strain corresponding to a bulk crystal, to simulate the effect of the computational domain being embedded in a large bulk specimen on all sides except the top free surface. Other alternatives led to spurious effects, e.g. traction-free all around allowed the entire specimen to bend due to the change in stress-free strain value at the top surface. The boundary conditions for the electrostatics (2.4)<sub>3</sub> are grounded on the top and side faces, and voltage decays as the distance from the specimen tends to infinity. A compensating charge is used on the free surface, its value corresponding to the bound charge due to normal termination of the polarization when there is no external field. As the tip field is introduced, the compensating charge is held fixed at this value even as the polarization at the free surface evolves in response to the applied field. We start with an initial polarization field that we use to obtain the strain and electric potential from (2.4)<sub>2,3</sub>. We then update the polarization using (2.4)<sub>1</sub>. This process is repeated until convergence.

The polarization update (2.4)<sub>1</sub> and mechanical equilibrium (2.4)<sub>2</sub> both use standard finite element methods (FEM) with triangle elements and linear shape functions, and polarization and displacement are the primary variables respectively.

The electrostatic equation (2.4)<sub>3</sub> needs attention as the electric fields are not confined to the ferroelectric but extend over all space. We model the triangular tip with a uniform charge density  $\sigma$  above the specimen. Hence, it is important to account for the electric fields in vacuum and they cannot be neglected as they mediate the tip-ferroelectric interactions. We apply a Dirichlet-to-Neumann boundary element method to solve this infinite domain problem efficiently and accurately, as described in [17, 18]; in particular, [18] describes an iterative formulation that is particularly suited for nonlinear coupled problems such as arise here. While the details of the method are discussed in these references, the essential aspect of the method is that it consistently transforms the Neumann-type boundary conditions from the charge on the tip and the bound charge in the ferroelectric to the Dirichlet-type boundary conditions of potential specified on the boundary of the ferroelectric  $\Omega$ , Fig. 1. This enables us to then solve (2.4)<sub>3</sub> using standard FEM.

### 3 Domain Nucleation in a $c$ axis Film

In this section, we study the physics of domain nucleation in a  $c$  axis film as shown in Fig. 2. For the following, we note that tip strength  $\sigma$  is non-dimensionalized with spontaneous polarization of barium titanate and the thickness of the domain wall.

Fig. 2 shows the equilibrium domain patterns as the the tip strength increases. We see qualitative differences in the microstructural accommodation of the external field. For relatively small charge  $\sigma = 0.5$ , the magnitude of polarization in the region directly beneath the tip simply reduces due to the external electric field, Fig. 2(a). The transition to the bulk value is fairly smooth and the domain wall energy  $U$  is not significant. In Fig. 3(a), we see that the electric field has penetrated into the material up to a distance comparable to the height of the tip. The stress is similarly significant only in a small zone near the surface, Fig. 3(b).

As the charge is increased,  $\sigma = 0.75$ , we see a small amount of switching, Fig. 2(b). While the new domain is mechanically compatible with the surrounding domain, the head-to-head polarization is energetically unfavorable but is stabilized by the external electric field. We see the formation of two broad transition regions between these incompatible domains.

We then increase the tip strength to  $\sigma = 1.0$ . The domain patterns in Fig. 2(c) show the clear presence of a new  $c^-$  domain directly beneath the tip. The transition between the new domain and the original domain is mediated by two symmetric lobes that form roughly  $90^\circ$  domain walls between the other domains. These lobes are reminiscent of domain patterns calculated near crack tips, e.g. [27, 28, 26]. In addition, we see the extremely interesting feature that the new domain's piezoresponse causes it to elongate under the applied field, rather than contract as is the case for the embedding domain. This is clearly observable through the surface topography. Fig 2(d) shows this as a leveling off of the tip strength vs. displacement curve. With this new domain, we also find that the electric and stress fields are no longer localized beneath the tip but extend through much of the specimen, Figs. 3(c), 3(d). The bound charge due to the electrically incompatible head-to-head domains enables the electric field to penetrate well beyond the extent of the new domain. The highest stresses are no longer directly beneath the tip but follow the boundaries of the lobes that separate the new and original domains.

### 4 Domain Nucleation in Films with $a$ axis and Other Free-Surface Orientations

In this section, we study the physics of domain nucleation for different crystal lattice orientations with respect to the free surface. We use  $\theta$  to indicate this orientation, i.e.,  $\theta$  is the angle between the free surface tangent and the crystal lattice, see Fig. 4. Hence, the  $c$  axis film of the previous section corresponds to  $\theta = 90^\circ$ .

We first examine the behavior of domain patterns under a small applied field,  $\sigma = 0.25$ , for various  $\theta$  as shown in Fig. 4. Even at small field, we notice qualitative differences. For smaller values of  $\theta$ , reduction in the magnitude of polarization is not significant; instead the polarization beneath the tip aligns with the applied field. In particular, for  $a$  axis ( $\theta = 0^\circ$ ), we find that the polarization rotates by  $90^\circ$  and forms a clear domain wall on one side. For smaller values of  $\theta$ , the results are qualitatively similar but less pronounced. For  $\theta = 45^\circ$ , and to some extent also for  $\theta = 30^\circ$ , we find the magnitude of polarization

decreasing as was observed in  $c$  axis films.

When  $\sigma = 0.5$ , Fig. 5, we see the formation of distinct  $c^-$  domains and clear  $90^\circ$  domain walls for  $\theta = 0^\circ$  and  $15^\circ$ . The magnitude of polarization in the new domain also increases to accommodate the applied field. The qualitative behavior for  $\theta = 35^\circ$  and  $45^\circ$  is similar to the  $c$  axis film. We also examine the electric field and stress in Figs. 6 and 7 for  $\sigma = 0.5$  and various  $\theta$ . The induced stress and electric fields both decrease as  $\theta$  increases. This can be understood from the fact that reduction of polarization magnitude is an available accommodation mechanism for larger  $\theta$ , whereas for smaller  $\theta$  a new  $c^-$  domain has to nucleate. As expected, Fig. 6 shows a larger field near the new domain due to electrically incompatible microstructures. Similarly, the stresses are also larger in the vicinity of the new domain, Fig. 7. In particular, Fig. 7(a) shows that a much higher stress occurs for  $\theta = 0$  due to the mechanically incompatible interface between domains on the left side of the new domain. Fig. 7(d) has a high stress region on the left near the surface, corresponding to the polarization switching shown in Fig. 8(d) and discussed below.

Finally, we examine the case with large tip charge,  $\sigma = 0.75$ , Fig. 8. The polarization magnitude increases in the new domain for  $\theta = 0^\circ$  and  $\theta = 15^\circ$ . However, for  $\theta = 30^\circ$  and  $\theta = 45^\circ$ , instead of a  $c^-$  domain with polarization aligned along the applied field, we instead see the new domain slightly tilted to orient itself along a crystallographically preferred direction.

We also note an unusual observation for  $\theta = 45^\circ$  and  $\theta = 60^\circ$ . Fig. 9 shows the polarization switching over a large region near the surface. For  $\sigma = 0.5$ , this region is large but limited in size, while for  $\sigma = 0.75$ , it extends to the boundary of the computational domain. The presence of a crystallographically equivalent preferred direction that is better oriented with respect to the applied field enables this large-scale domain switching. The domain wall between the original domain and the large switched region is both mechanically and electrically compatible. When  $\theta = 60^\circ$ , Fig. 10, we find a similar large-scale switching; the main qualitative difference with  $\theta = 45^\circ$  is that it occurs at a lower value of applied field and the domain wall is better defined.

## 5 Conclusion

We have studied the process of domain switching and nucleation at a free surface under an applied electric field through a tip above the surface. We have used a real-space phase-field model in combination with a boundary element method that enables us to accurately resolve the stray electric fields as well as the interaction between the tip and the sample through these stray electric fields. We have applied this to calculate domain patterns and the process of nucleation as the applied field is increased. We have also examined the effect of different orientations of the crystal lattice with respect to the free surface. In the cases of  $a$  and  $c$  axes films that have been studied experimentally, the surface response matches qualitatively with experimental measurements [29]. Quantitative comparisons will require more careful consideration of many effects, e.g. pinning defects, that we have not considered here.

In the  $c$  axis film, we find significant differences between our calculations of domain patterns and simplified analytical approximations that are often used to understand the nucleation process assumed, e.g. [8]. We also find that once a new domain nucleates, the piezoelectric response of the new domain cancels to some extent with the original domain. The surface topography has an interesting and distinctive ‘‘bump’’ as a signature of this effect. In addition, this causes the tip displacement as a function of applied field to level off. The latter consequence is directly amenable to experimental observation.

In our calculations of nucleation process as a function of relative lattice orientation, we find some general trends. Particularly, domain nucleation occurs at lower applied fields for small values of relative lattice orientation, i.e.,  $a$  axis films nucleate new domains under smaller field when compared to  $\theta = 30^\circ$ , and  $30^\circ$  nucleates a new domain under smaller field than  $45^\circ$ , and so on. This was understood physically as a competition between two mechanisms to accommodate the applied field. One mechanism, favored in  $a$  axis films and smaller relative lattice orientations, is for the polarization to rotate and align itself with the applied field, thus leading to a new domain. The other mechanism, favored in  $c$  axis films and larger relative lattice orientations, is for the magnitude of the polarization to reduce without changing direction for smaller field, and then switch by  $180^\circ$  for sufficiently large field. We also observed that the presence of crystallographically equivalent preferred directions can lead to large scale surface switching in films as yet another mechanism to align the polarization with the applied field. While there have been a number of experiments to characterize domain nucleation behavior in  $a$  and  $c$  axis films [30], there has been much less effort in other orientations. Comparative analyses through experiment offers a route to validate some of our findings.

## Acknowledgment

This research was supported in part by the National Science Foundation through TeraGrid resources provided by the Pittsburgh Supercomputing Center. The real-space phase-field program that we have developed to obtain the results described in this paper is available at [www.matforge.org](http://www.matforge.org).

## References

- [1] Y. Xu. *Ferroelectric materials and their applications*. North-Holland, 1991.
- [2] K. Uchino. *Piezoelectric Actuators and Ultrasonic Motors*. Kluwer, 1996.
- [3] J.F. Scott. *Ferroelectric memories*. Springer Verlag, 2000.
- [4] A. K. Tagantsev, V. O. Sherman, K. F. Astafiev, J. Venkatesh, and N. Setter. Ferroelectric materials for microwave tunable applications. *J. Electroceram.*, 11:5–66, 2003.
- [5] M. Y. El-Naggar, K. Dayal, D. G. Goodwin, and K. Bhattacharya. Graded ferroelectric capacitors with robust temperature characteristics. *J. Appl. Phys.*, 100:114115, 2006.
- [6] K. Dayal and K. Bhattacharya. Active tuning of photonic device characteristics during operation by ferroelectric domain switching. *J. Appl. Phys.*, 102:064102, 2007.
- [7] B.W. Wessels. Ferroelectric epitaxial thin films for integrated optics. *Annu. Rev. Mater. Res.*, 37:659–679, 2007.
- [8] S. Jesse, A.P. Baddorf, and S.V. Kalinin. Switching spectroscopy piezoresponse force microscopy of ferroelectric materials. *Applied physics letters*, 88:062908, 2006.
- [9] S.V. Kalinin, A. Rar, and S. Jesse. A decade of piezoresponse force microscopy: progress, challenges, and opportunities. *Ultrasonics, Ferroelectrics and Frequency Control, IEEE Transactions on*, 53(12):2226–2252, 2006.

- [10] J. Li, P.T. Lin, and BW Wessels. Polarization reversal and backswitching dynamics in epitaxial batio<sub>3</sub> thin films. *Journal of Applied Physics*, 106(5):054113–054113, 2009.
- [11] J. Li, Z. Liu, and BW Wessels. Study of domain reversal and its field-dependence in epitaxial batio<sub>3</sub> thin films. *Journal of Applied Physics*, 107(12):124106–124106, 2010.
- [12] A.N. Morozovska, E.A. Eliseev, and S.V. Kalinin. Domain nucleation and hysteresis loop shape in piezoresponse force spectroscopy. *Applied physics letters*, 89:192901, 2006.
- [13] A.N. Morozovska, S.V. Svechnikov, E.A. Eliseev, B.J. Rodriguez, S. Jesse, and S.V. Kalinin. Local polarization switching in the presence of surface-charged defects: Microscopic mechanisms and piezoresponse force spectroscopy observations. *Physical Review B*, 78(5):054101, 2008.
- [14] S.V. Kalinin, A. Gruverman, and D.A. Bonnell. Quantitative analysis of nanoscale switching in SrBiTaO thin films by piezoresponse force microscopy. *Applied physics letters*, 85:795, 2004.
- [15] A.N. Morozovska, E.A. Eliseev, and S.V. Kalinin. The piezoresponse force microscopy of surface layers and thin films: Effective response and resolution function. *Journal of Applied Physics*, 102(7):074105–074105, 2007.
- [16] N. Ng, R. Ahluwalia, HB Su, and F. Boey. Lateral size and thickness dependence in ferroelectric nanostructures formed by localized domain switching. *Acta Materialia*, 57(7):2047–2054, 2009.
- [17] K. Dayal and K. Bhattacharya. A real-space non-local phase-field model of ferroelectric domain patterns in complex geometries. *Acta materialia*, 55(6):1907–1917, 2007.
- [18] Lun Yang and Kaushik Dayal. A completely iterative method for the infinite domain electrostatic problem with nonlinear dielectric media. *Journal of Computational Physics*, 230(21):7821 – 7829, 2011.
- [19] YC Shu and K. Bhattacharya. Domain patterns and macroscopic behaviour of ferroelectric materials. *Philosophical Magazine Part B*, 81(12):2021–2054, 2001.
- [20] LJ Li, CH Lei, YC Shu, and JY Li. Phase-field simulation of magnetoelastic couplings in ferromagnetic shape memory alloys. *Acta Materialia*, 2011.
- [21] LJ Li, Y. Yang, YC Shu, and JY Li. Continuum theory and phase-field simulation of magnetoelectric effects in multiferroic bismuth ferrite. *Journal of the Mechanics and Physics of Solids*, 58(10):1613–1627, 2010.
- [22] W. Zhang and K. Bhattacharya. A computational model of ferroelectric domains. Part I: model formulation and domain switching. *Acta materialia*, 53(1):185–198, 2005.
- [23] Lun Yang and Kaushik Dayal. Effect of lattice orientation, surface modulation, and applied fields on free-surface domain microstructure in ferroelectrics. *Acta Materialia*, 59(17):6594 – 6603, 2011.
- [24] L. Yang and K. Dayal. Formulation of phase-field energies for microstructure in complex crystal structures. *Applied Physics Letters*, 96:081916, 2010.
- [25] Y. Xiao, V.B. Shenoy, and K. Bhattacharya. Depletion layers and domain walls in semiconducting ferroelectric thin films. *Physical review letters*, 95(24):247603, 2005.

- [26] Lun Yang and Kaushik Dayal. Microstructure and stray electric fields at surface cracks in ferroelectrics. *submitted*, 2011.
- [27] Amir Abdollahi and Irene Arias. Phase-field modeling of the coupled microstructure and fracture evolution in ferroelectric single crystals. *Acta Materialia*, 59(12):4733 – 4746, 2011.
- [28] J. Wang and T.Y. Zhang. Phase field simulations of polarization switching-induced toughening in ferroelectric ceramics. *Acta materialia*, 55(7):2465–2477, 2007.
- [29] S.V. Kalinin, B.J. Rodriguez, S. Jesse, E. Karapetian, B. Mirman, E.A. Eliseev, and A.N. Morozovska. Nanoscale electromechanics of ferroelectric and biological systems: A new dimension in scanning probe microscopy. *Annu. Rev. Mater. Res.*, 37:189–238, 2007.
- [30] S. Kalinin and A. Gruverman. *Scanning probe microscopy: Electrical and electromechanical phenomena at the nanoscale*, volume 1. Springer Verlag, 2007.



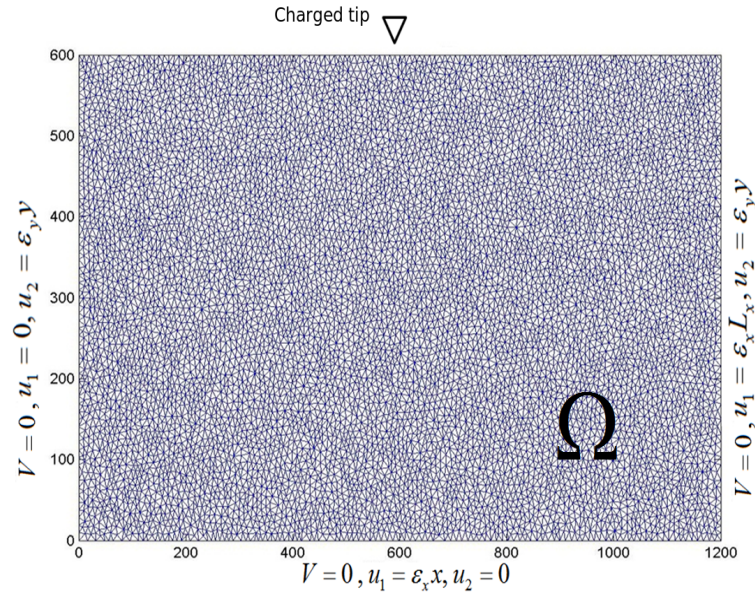


Figure 1: Computational domain and tip geometry, mesh, and boundary conditions. Length units are nanometers, and the lengthscale of the domain wall width is roughly 25nm. The boundary conditions for the polarization is  $\mathbf{p} \cdot \hat{\mathbf{n}}$  on all boundaries.  $\epsilon_x, \epsilon_y$  correspond to the stress-free strains of the bulk crystal. Numerical experiments with finer meshes and larger specimen sizes suggest that the results are converged with the chosen values.

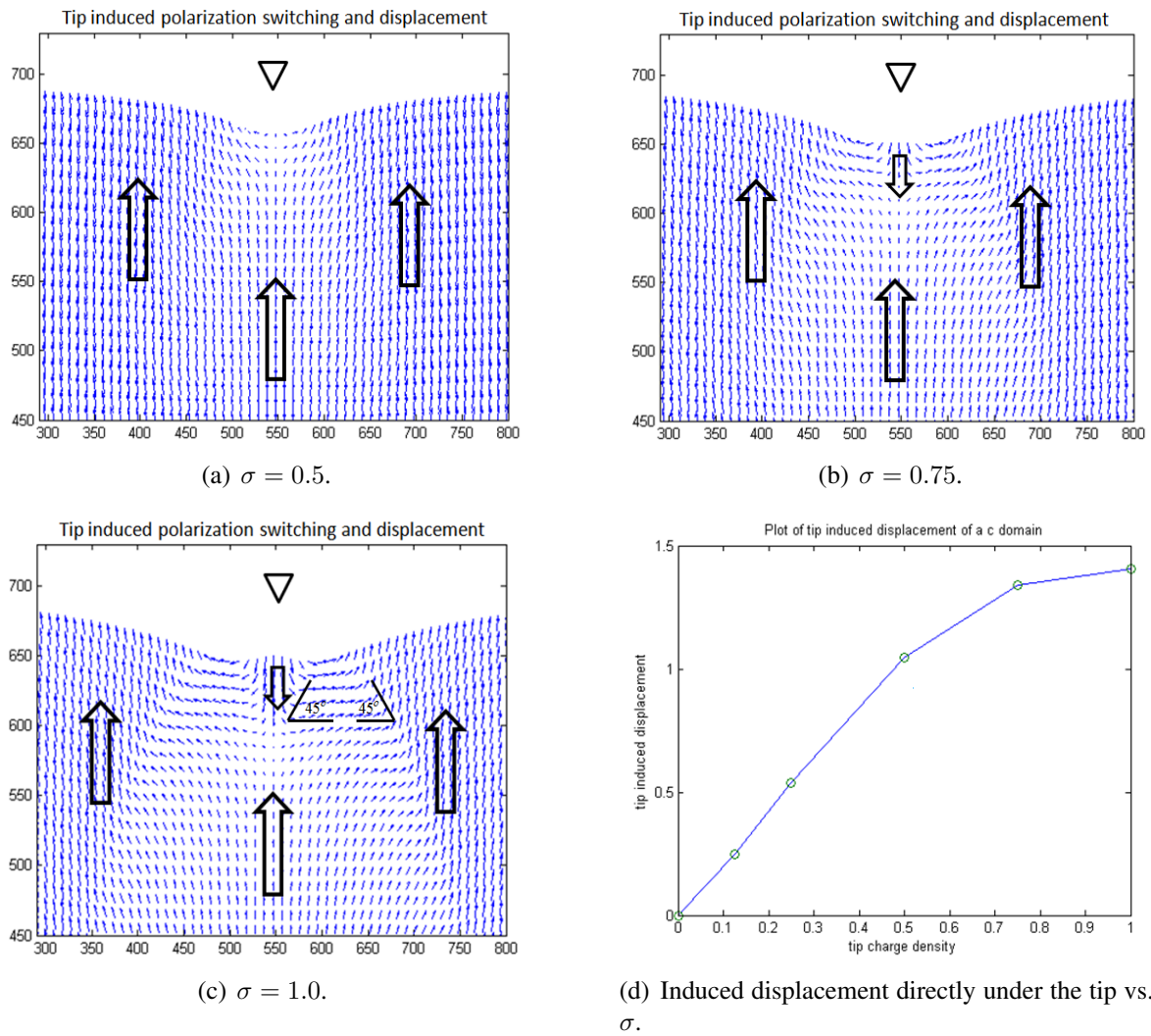


Figure 2: Polarization and induced displacement of a *c* domain under a tip with charge  $\sigma$ .

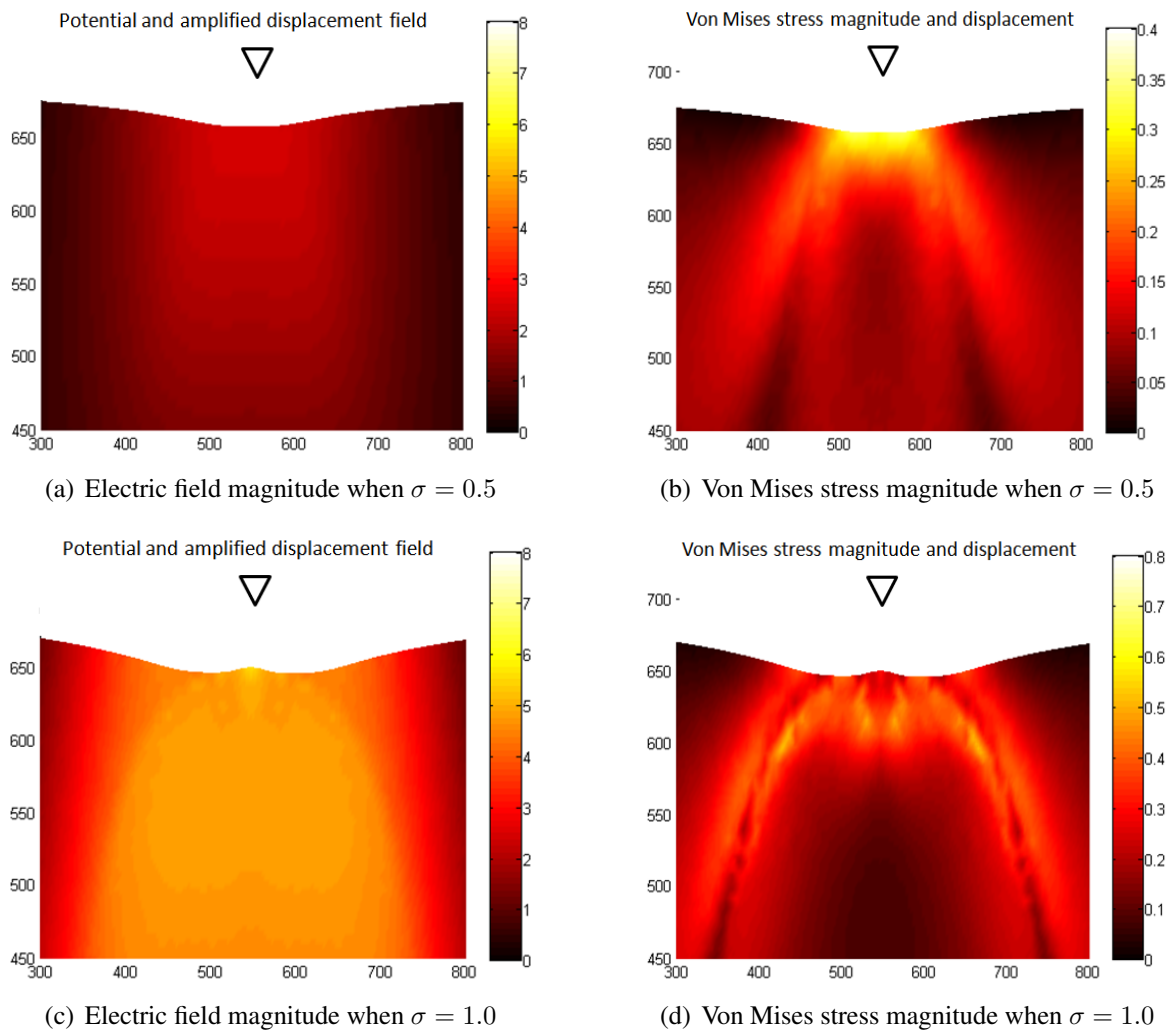


Figure 3: Von Mises stress and electric field magnitude of a  $c$  axis film under a tip with charge density  $\sigma$ .

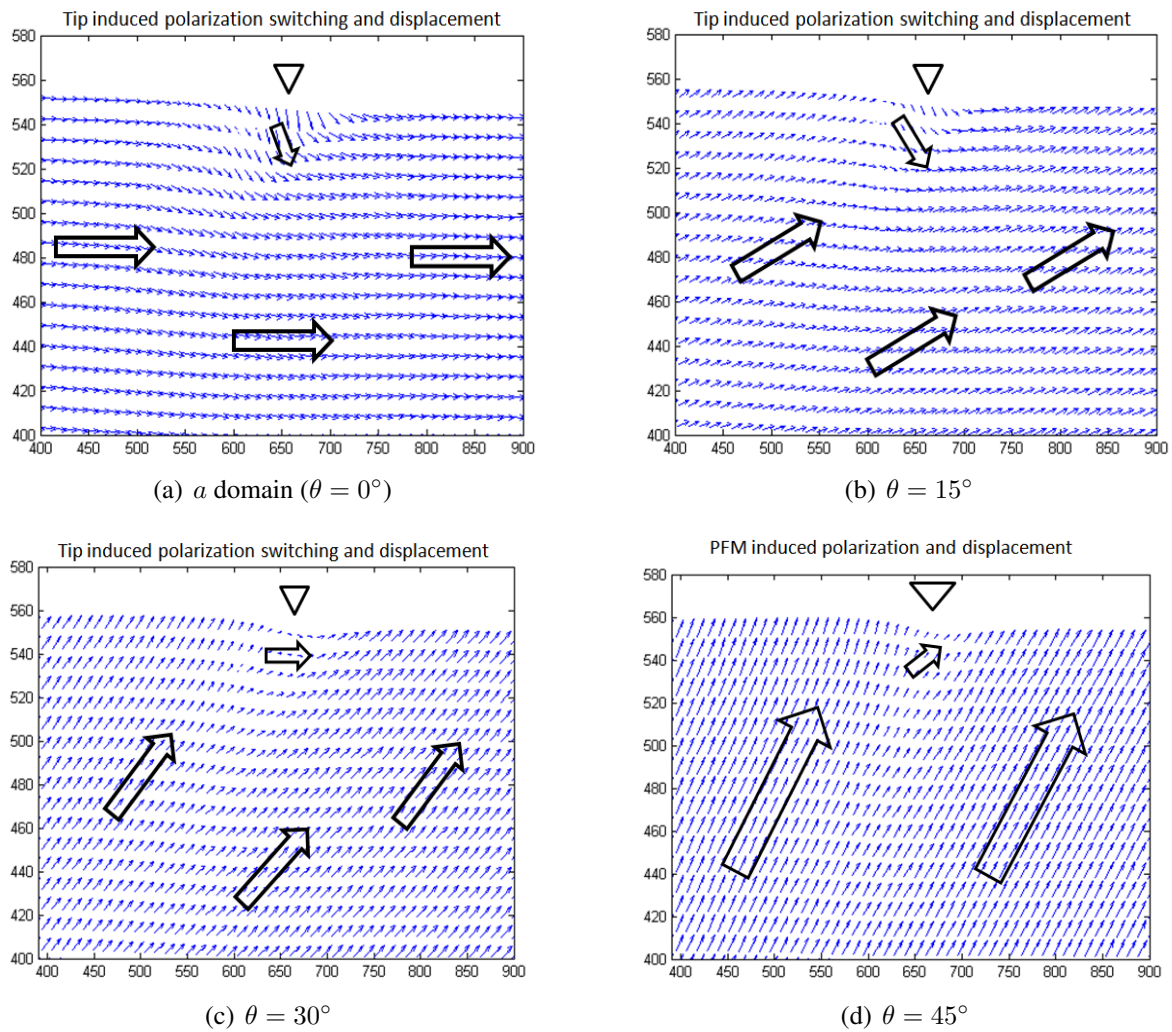


Figure 4: Polarization field and induced displacement for various lattice orientations  $\theta$  with tip charge  $\sigma = 0.25$ .

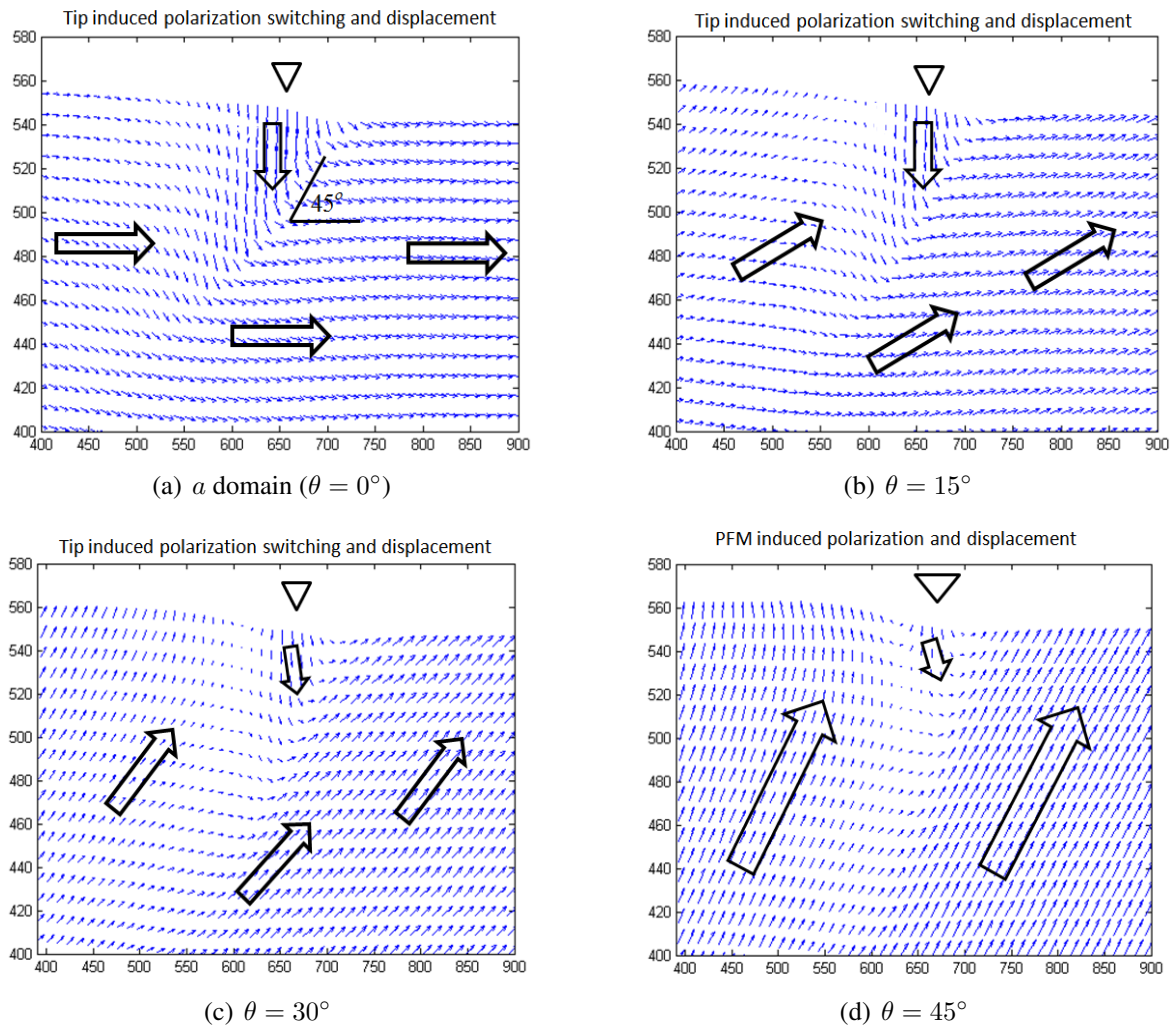


Figure 5: Polarization field and induced displacement for various lattice orientations  $\theta$  with tip charge  $\sigma = 0.5$ .

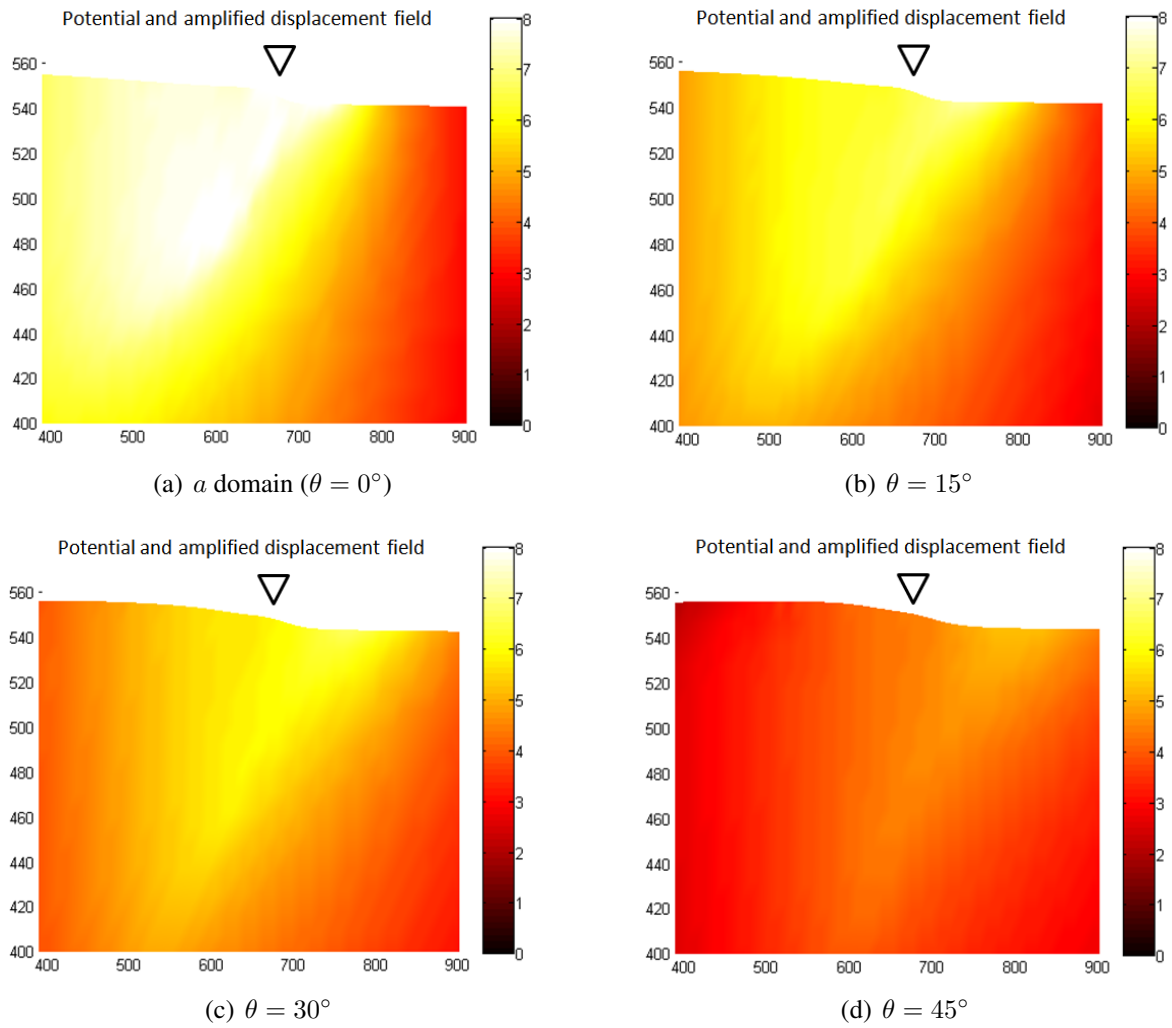


Figure 6: Potential field for various lattice orientations  $\theta$  with tip charge  $\sigma = 0.5$ .

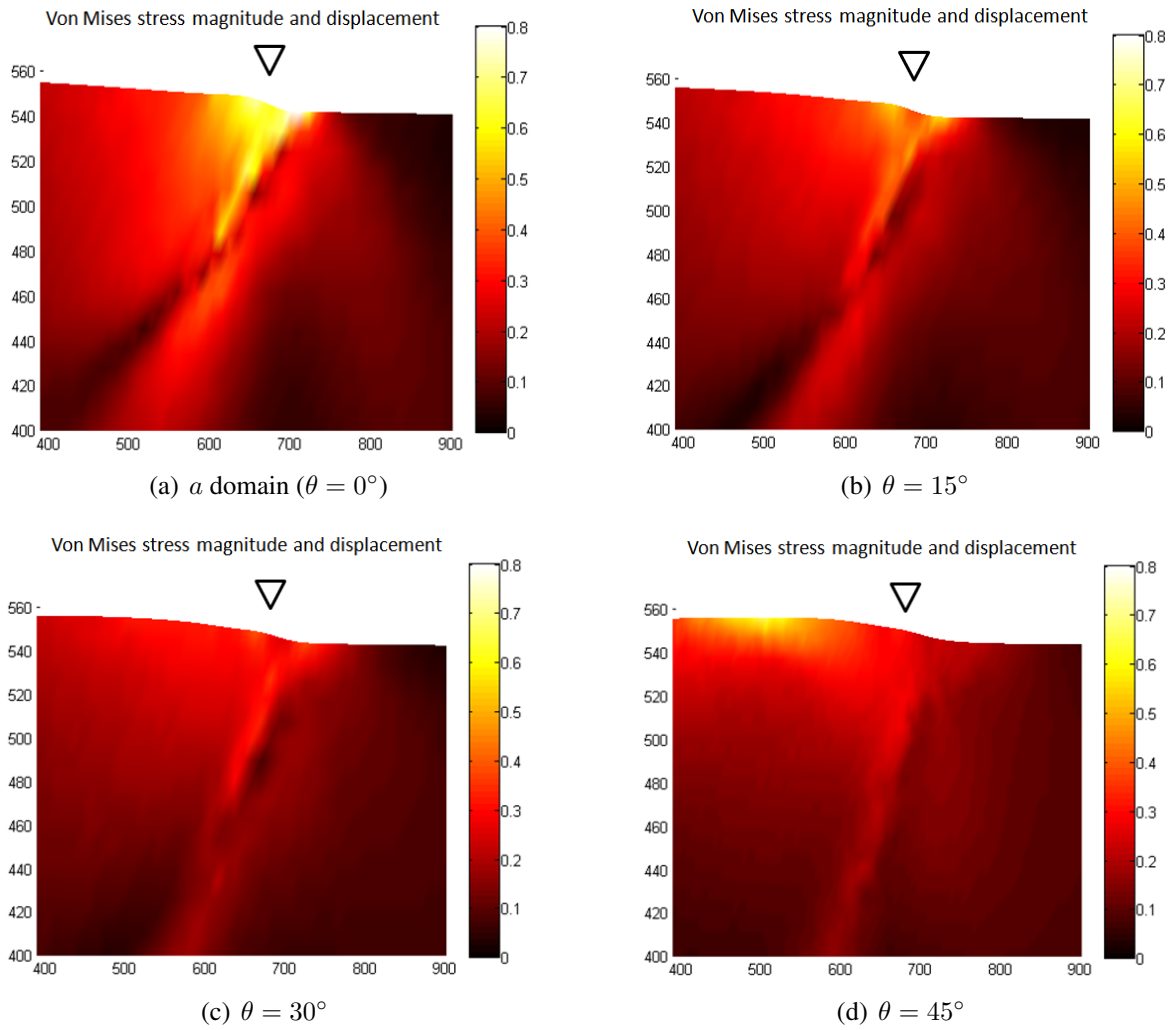


Figure 7: Von Mises stress field for various lattice orientations  $\theta$  with tip charge  $\sigma = 0.5$ .

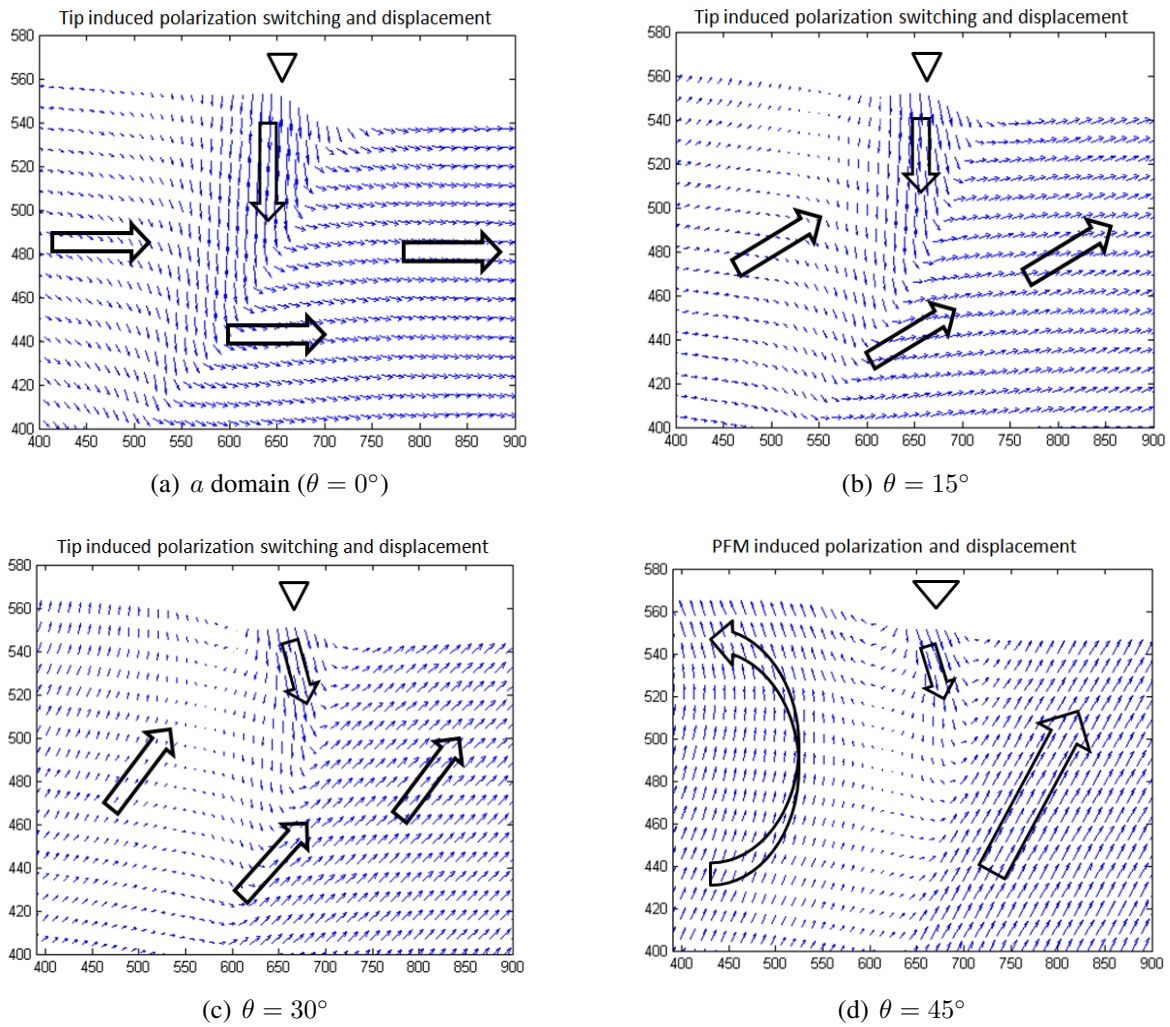


Figure 8: Polarization field and induced displacement for various lattice orientations  $\theta$  with tip charge  $\sigma = 0.75$ .

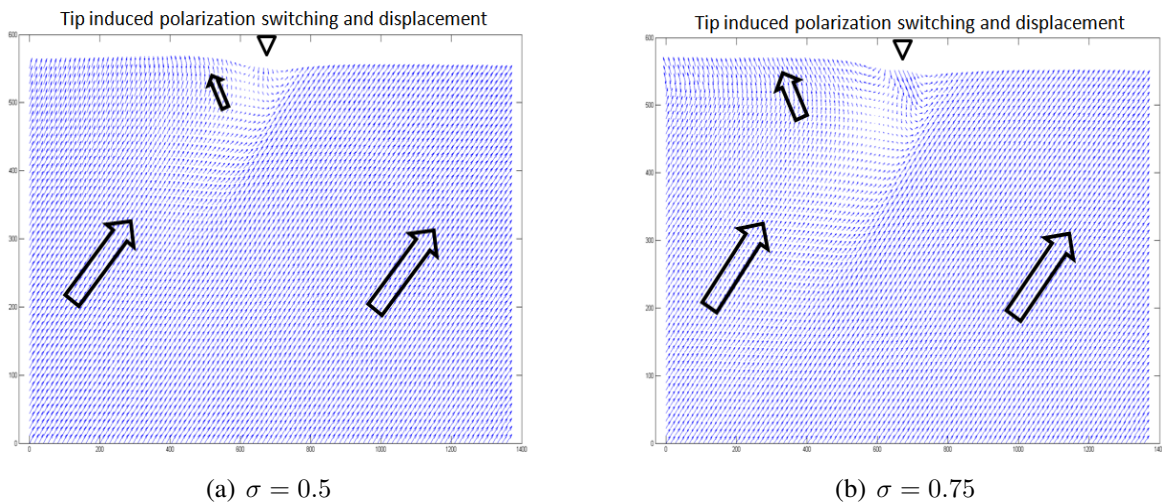


Figure 9: Domain patterns and induced displacement field when  $\theta = 45^\circ$  showing polarization switching near the surface for different tip charges  $\sigma$ .



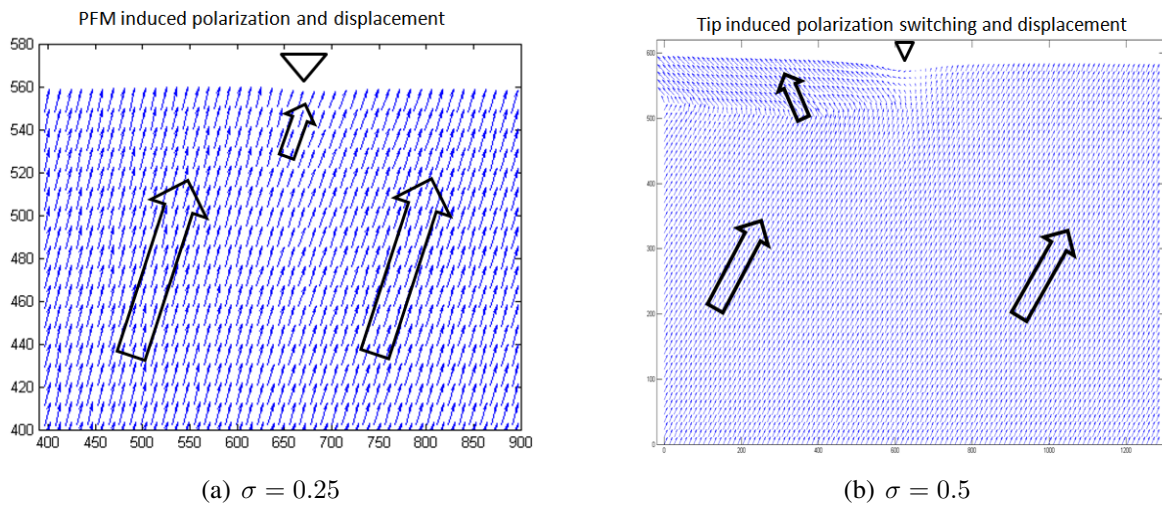


Figure 10: Domain patterns and induced displacement field when  $\theta = 60^\circ$  showing polarization switching near the surface for different tip charges  $\sigma$ .